Research Article

Nano Research
2022, 15(10): 9588–9594

ISSN 1998-0124 CN 11-5974/O4
https://doi.org/10.1007/s12274-022-4580-3

Observation of interlayer excitons in trilayer type-II transition metal dichalcogenide heterostructures

Biao Wu[1,2], Haihong Zheng[1,2], Junnan Ding[1,2], Yunpeng Wang[1], Zongwen Liu[3], and Yanping Liu[1,2,4] (✉)

[1] *School of Physics and Electronics, Hunan Key Laboratory for Super-microstructure and Ultrafast Process, Central South University, Changsha 410083, China*
[2] *State Key Laboratory of High-Performance Complex Manufacturing, Central South University, Changsha 410083, China*
[3] *School of Chemical and Biomolecular Engineering, The University of Sydney, NSW 2006, Australia*
[4] *Shenzhen Research Institute of Central South University, Shenzhen 518057, China*

Received: 10 May 2022 / **Revised:** 23 May 2022 / **Accepted:** 24 May 2022

ABSTRACT

Vertically stacked transition metal dichalcogenide (TMD) heterostructures provide an opportunity to explore optoelectronic properties within the two-dimensional limit. In such structures, spatially indirect interlayer excitons (IXs) can be generated in adjacent layers because of strong Coulomb interactions. However, due to the complexity of the multilayered heterostructure (HS), the capture and study of the IXs in trilayer type-II HSs have so far remained elusive. Here, we present the observation of the IXs in trilayer type-II staggered band alignment of $MoS_2/MoSe_2/WSe_2$ van der Waals (vdW) HSs by photoluminescence (PL) spectroscopy. The central energy of IX is 1.33 eV, and the energy difference between the extracted double peaks is 23 meV. We confirmed the origin of IX through PL properties and calculations by the density functional theory, we also studied the dependence of the IX emission peak on laser power and temperature. Furthermore, the polarization-resolved PL spectra of HS were also investigated, and the maximum polarizability of the emission peak of WSe_2 reached 11.40% at 6 K. Our findings offer opportunities for the study of new physical properties of excitons in TMD HSs and therefore are valuable for exploring the potential applications of TMDs in optoelectronic devices.

KEYWORDS

transition metal dichalcogenides, interlayer exciton, type-II band alignment, trilayer heterostructure

1 Introduction

Two-dimensional (2D) transition metal dichalcogenides (TMDs) have attracted widespread attention because of their unique electronic and optical properties that have wide application perspectives in the fields of electronics and optoelectronics [1–7]. The vertical stacking of two different monolayered TMDs can form a van der Waals (vdW) heterostructure (HS), creating interesting new characteristics that are different from that of the monolayer structures [8–10]. For the vdW HS, the band arrangement of the various monolayer TMDs determines the properties and applications of the HS [11–15]. In the bilayer HS with a type-II band alignment, carriers are transferred from the high-energy layer to the low-energy layer due to the energy difference between the two TMD materials, and the formation of interlayer excitons (IXs) could be the driving force for light-excited electrons and holes to separate into different layers [16]. The IXs formed by the space-separated carriers due to the Coulomb effect have a significantly longer lifetime than their intralayer counterparts [1, 17]. Consequently, TMD HSs have wide-ranging application perspectives in long-life exciton devices and exciton quantum gas research [18–20].

Recently, many studies are focused on the HSs composed of two different monolayer TMDs [21–24]. Nevertheless, our interest is to design an embedded trilayer vertical heterostructure with type-II band alignment, and explore whether different layers can cause indirect–direct bandgap transitions. Compared to bilayer type-II HSs, the photoluminescence (PL) quantum efficiency and tunable spectral resonance of the trilayer HSs are considerably improved [13]. In addition, the IXs have a lower energy limit and a longer lifetime expectancy [25]. The trilayer vdW HSs of TMDs may have tremendous application potential such as photodetectors, light-emitting diodes, lasers, and photovoltaics [26–28]. However, the feature of IXs is only observed in the bilayer type-II heterostructures.

In this study, we were successful in fabricating a trilayer $MoS_2/MoSe_2/WSe_2$ HS encapsulated with hexagonal boron nitride (hBN) by dry transfer technique [29, 30]. By analyzing the PL spectrum, the IXs of the trilayer type-II $MoS_2/MoSe_2/WSe_2$ HS were observed. According to the energy range of the IXs, and the energy difference between the two peaks of IXs extracted by Lorentzian fitting is 23 meV. Therefore, the observed IXs were attributed to the $MoSe_2/WSe_2$ bilayer. The power dependence measurement indicated that the splitting of the IX was caused by the conduction band spin-splitting of $MoSe_2$. Furthermore, we also studied the circular polarization of the HS, and the maximum polarization rate of the WSe_2 emission peak reached 11.40% at 6 K. The results of the observation provide new insights for exploring new exciton physics and quantum emitters in TMDs materials.

Address correspondence to liuyanping@csu.edu.cn

2 Results and discussion

Figure 1(a) is an optical micrograph of the trilayer HS sample, with dashed outlines in different colors indicating regions of different materials. Figure 1(b) displays the schematic diagram of the HS, where hBN is placed on the top and bottom of the $MoS_2/MoSe_2/WSe_2$ HS. The HS is encapsulated with hBN to reduce scattering from the substrate and protect monolayer materials. The band arrangement diagram of the embedded $MoS_2/MoSe_2/WSe_2$ HS with type II is shown in Fig. 1(c). Carriers will transfer from high energy levels to low energy levels due to the energy difference between the monolayer materials. It can be seen from the schematic that the holes in the valence band of the adjacent layer are transferred to the upper layer, while the electrons in the conduction band are transferred to the lower layer. The middle layer acts as an intermediate medium for carrier transfer. The embedded type-II band alignment promotes carrier separation in type-II band alignment. The Raman spectrum of each layer constituting the HS is shown in Fig. 1(d). For monolayer WSe_2 [31], the out-of-plane A_{1g} and in-plane E^1_{2g} Raman modes were not degenerate under 532 nm excitation at room temperature, resulting in a split of 11–12 cm^{-1}. For monolayer $MoSe_2$, the observation result of the out-of-plane Raman mode signal is 240.5 cm^{-1}, which is consistent with that of previous reports [32]. For monolayer MoS_2 [33], the frequency difference between the A_{1g} and E^1_{2g} modes is less than 20 cm^{-1}. It can be observed that the Raman spectrum of the HS area contains all the vibration modes of the three materials, indicating that the three materials were well coupled. PL spectra were used to characterize MoS_2, $MoSe_2$, and WSe_2 monolayers, as well as the HS. Figure 1(e) presents the PL spectra of different monolayer and the HS regions excited by a 532 nm (2.33 eV) laser at room temperature. The central energies of the emission peaks of MoS_2, $MoSe_2$, and WSe_2 monolayers at room temperature are 1.83, 1.57, and 1.65 eV, respectively, which are consistent with previous reports [34–36]. Characteristic peaks for different monolayers were observed in the PL spectra of the HS region. Figure 1(f) shows the PL spectra of these monolayers and the HS region when the sample was cooled to 6 K. It can be observed that the PL spectra of the MoS_2, $MoSe_2$, and WSe_2 monolayers have strong peaks at 1.91, 1.61, and 1.67 eV, respectively, while the PL spectrum of the HS region has a peak at 1.33 eV, which is closely related to the peak of the IXs [1, 23].

To investigate the optical characteristics of the HS, we studied the PL spectra of MoS_2, $MoSe_2$, and WSe_2 monolayers, as well as the HS as a function of temperature, ranging from 6 to 300 K. It can be seen from Fig. 2 that as the temperature decreased, the types of the emission peaks of the TMD materials became more abundant, caused by suppressing the thermal disturbance of the electrons. Furthermore, as the temperature cooled down, the peak positions of all emission peaks were blue-shifted, which was consistent with the Varshni equation describing the change of the bandgap of traditional semiconductors with temperature [37]. The formula is as follows (Eq. (1))

$$E_g(T) = E_0 - \alpha T^2/(T+\beta) \quad (1)$$

where α and β are the fitting parameters of the Varshni equation, while $E_g(T)$ and E_0 represent the bandgaps at the current temperature and the absolute zero, respectively.

Figure 2(a) depicts the PL spectrum of the monolayer MoS_2 as a function of temperature. As the temperature went down, one peak became two peaks, and the peak positions of all emission peaks were blue-shifted. The types of these two excitons can be identified by their PL spectra [34]. The central energies of the two emission peaks at 6 K are 1.799 and 1.907 eV, respectively, which are expressed as bound exciton (X_L) and neutral exciton (X_0). Interestingly, the measurement showed that the peak of bound

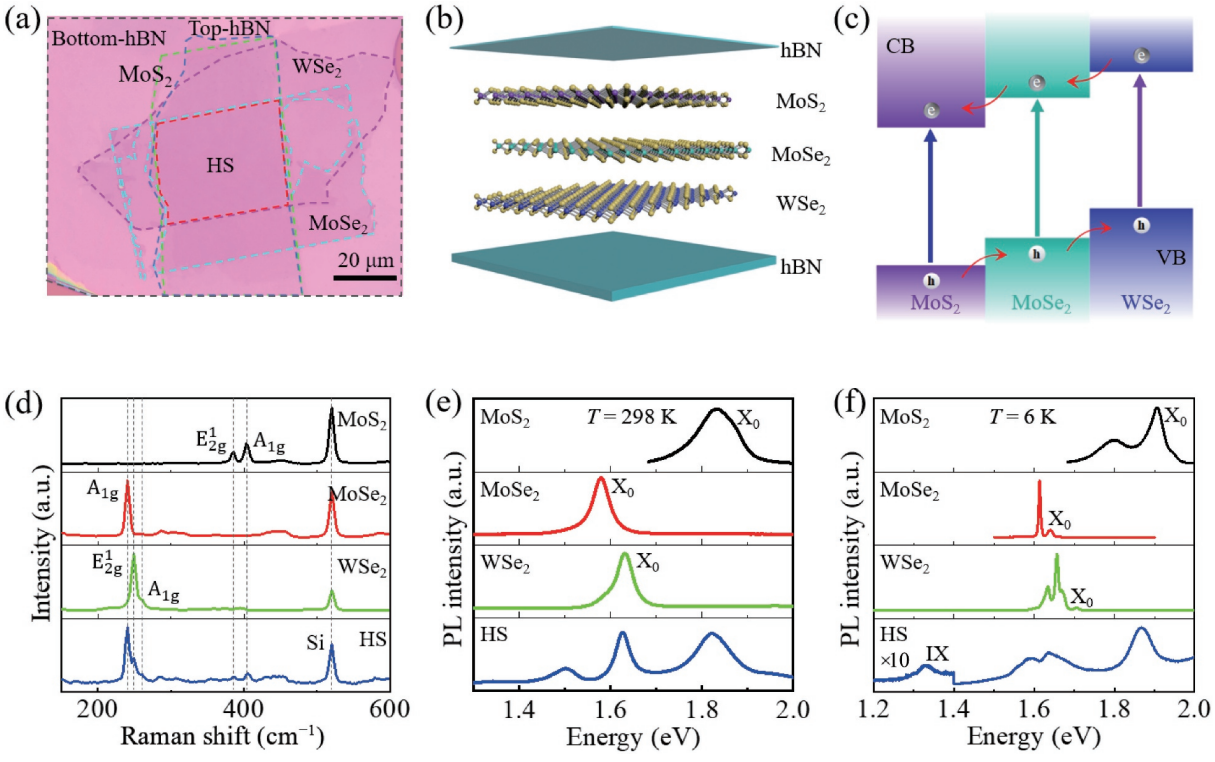

Figure 1 Design and characterization of the $MoS_2/MoSe_2/WSe_2$ HS. (a) Optical micrograph of $MoS_2/MoSe_2/WSe_2$ HS encapsulated with hBN. The dashed lines indicate different materials in different areas. (b) Schematic diagram of the $hBN/MoS_2/MoSe_2/WSe_2/hBN$ HS. (c) Schematic diagram of the energy band of the HS. The arrows of different colors indicate the formation of different direct excitons, and the elliptical dashed box indicates the formation of IXs. The red arrows indicate the transfer process of carriers in different layers. (d) Raman spectra of single materials and HS at room temperature. (e) and (f) represent the PL spectra of MoS_2, $MoSe_2$, WSe_2, and HS under excitation at 532 nm at room temperature (298 K) and 6 K, respectively.

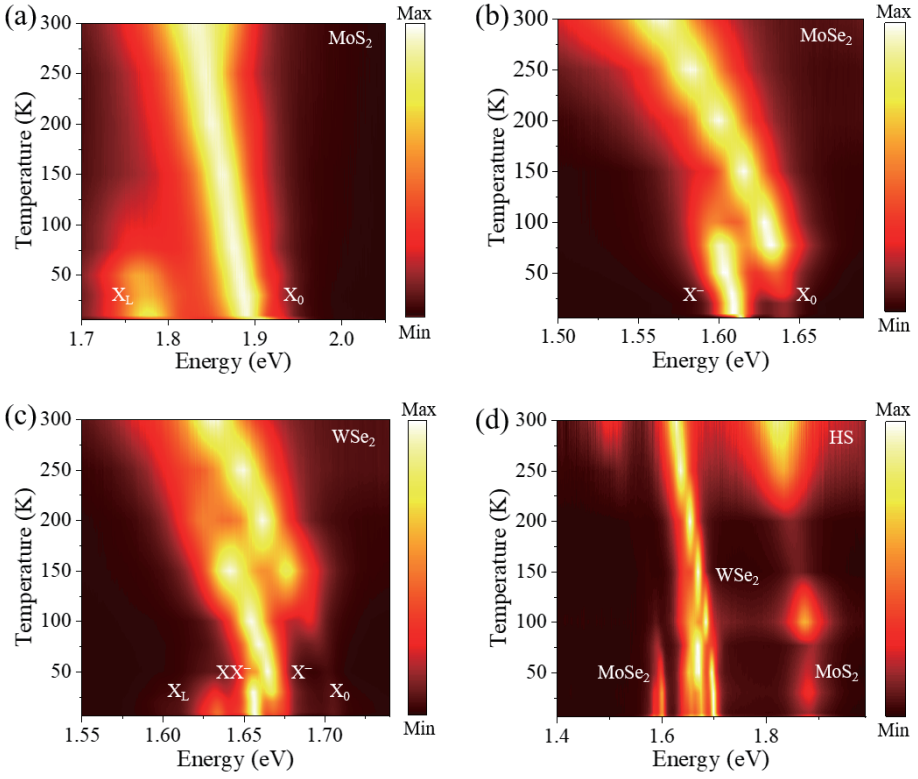

Figure 2 Temperature-dependent PL maps. The temperature dependence PL of (a) monolayer MoS_2, (b) monolayer $MoSe_2$, (c) monolayer WSe_2, and (d) HS, varying from 6 to 300 K. The exciton type corresponding to each PL peak is marked on the corresponding heat map. (d) The emission peaks of various materials in the HS are also marked with the corresponding materials. As the temperature decreases, the emission peak appears blue-shifted, which is consistent with the Varshni equation of traditional semiconductors.

exciton appeared at an energy below 1.85 eV, suggesting that there might be a large number of defects distributed in the monolayer MoS_2, which acted as the trap sites for excitons. The trapped electrons are combined with holes to form defect-bound excitons. Therefore, multiple defect energy levels appeared in the energy bandgap to produce a broad X_L peak. Figure 2(b) shows the variation of the PL spectrum of the monolayer $MoSe_2$ in relation to temperature. It should be noted that as the temperature cooled down, the primary peak splited into two peaks, and the emission peaks are blue-shifted. At 6 K, the position energy difference of the two emission peaks is 27 meV, which is similar to previous reports [21]. These two emission peaks are represented as X_0 and charged exciton (X^-) of monolayer $MoSe_2$, respectively. In addition, when the temperature was below 77 K, it could be seen that the X^- peak gradually dominated, while the X_0 peak became weaker, which was caused by the limitation of electronic thermal fluctuations [38]. Similarly, Fig. 2(c) shows the PL spectrum of the monolayer WSe_2 versus temperature. It could be observed that as the temperature decreased, the types of excitons of the monolayer WSe_2 became very abundant [39, 40]. At 6 K, the energies of the low to high emission peaks are depicted as X_L, charged biexciton (XX^-), X^-, and X_0 [16]. Figure 2(d) illustrates the variation of the PL spectra of the $MoS_2/MoSe_2/WSe_2$ HS with temperature. The PL spectra of the three materials can be clearly distinguished from the PL spectrum of the HS, with the emission peaks displaying a blue shift as the temperature decreased.

To explore the properties of the IXs, we carried out detailed research and discussions in Fig. 3. As shown in Fig. 3(a), as the temperature decreases, the peak intensity of the IX increases due to the decrease in the thermal disturbance and scattering of the electrons, and the peak position appears blue shifted [37]. When the temperature is below 77 K, two peaks of IX emission can be slightly observed, which can be caused by IX splitting due to the spin–orbit coupling effect [1]. It is worth noting that the energy of the IX emission peak ranges from 1.26 to 1.38 eV at 6 K. According to the characteristics of the IX emission peak, it can be related to the IX emission peak of the $MoSe_2/WSe_2$ bilayer [41, 42]. Figure 3(b) shows the IX peak in the HS region at 6 K excited by a 532 nm laser. The observed IX peak was deconvoluted into two peaks, IX_1 and IX_2, by Lorentzian function fitting. Importantly, it can be observed that the energies of the IX_1 and IX_2 peaks are 1.327 and 1.350 eV, respectively, having the energy difference of 23 meV that is entirely consistent with the first-principle calculations on the splitting of the $MoSe_2$ conduction band [43]. It was theoretically predicted that the conduction band splitting of MoS_2 is only 3 eV and the binding energy of the negative interlayer trion is 28 eV, so the observed interlayer excitons cannot come from the $MoS_2/MoSe_2$ bilayer [21, 43]. Furthermore, the low IX energy of the MoS_2/WSe_2 bilayer is beyond the detection range of our device (1.1–2.2 eV) [44]. Therefore, the observed interlayer excitons originate from the $MoSe_2/WSe_2$ bilayer. Consequently, the splitting of the IX is most likely to originate from the splitting of the $MoSe_2$ conduction band.

Figure 3(c) shows the heat map of the IXs at 6 K as a function of the laser power. The data was derived from Fig. 3(d), making the evolution of IXs with power more intuitive. It can be observed that as the power increased, the peaks of the IXs also became stronger. At the same time, Fig. 3(d) displays the normalized PL intensity of IXs at 6 K as a function of the laser power, varying from 0.1 to 5 mW. Under the power of 0.1 and 5 mW, the PL spectra of IX_1 and IX_2 were obtained by Lorenzian function fitting, represented by the blue and red lines, respectively. The arrowed directions of the blue and red dotted lines were the evolution of IX_1 and IX_2 with the excitation power. Interestingly, as the power increased, the IX_1 peak gradually weakened, whereas the IX_2 peak became stronger gradually. The observed dipole phenomenon is in line with the spin splitting of the monolayer $MoSe_2$ conduction

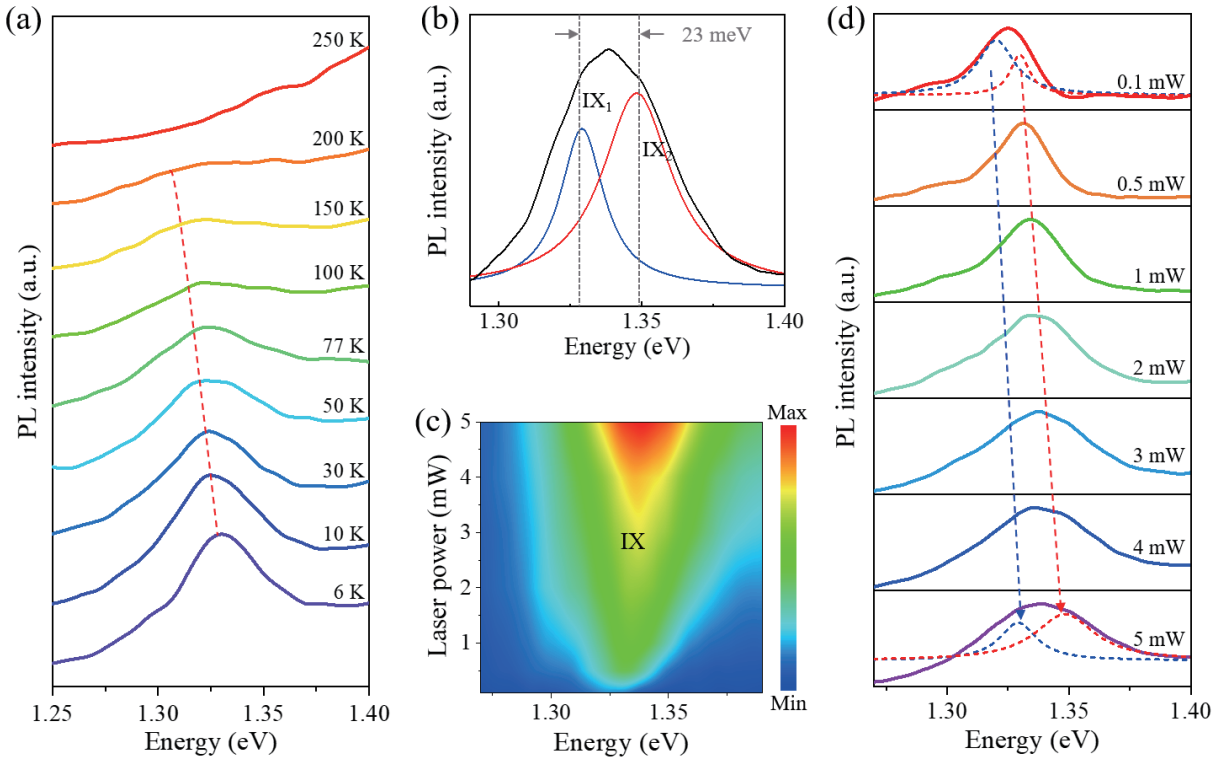

Figure 3 PL features of the HS. (a) PL spectra of IXs in the HS at varying temperatures. (b) The solid black line represents the measured data at 6 K, and the blue and red solid lines are the fitting peaks of IX_1 and IX_2, respectively. (c) The heat map of IXs as a function of power with the same data from (d). (d) The PL spectra of IXs at different excitation power range from 0.1 to 5 mW. At the power of 0.1 and 5mW, the PL spectra of IX_1 and IX_2 obtained by Lorentzian fitting were shown by blue and red lines, respectively. The blue and red dotted arrows are the evolution of IX_1 and IX_2 under different powers, respectively.

band. At low power, photo-excited electrons first filled the lowest energy configuration within the $MoSe_2$ spin splitting band, so that the IX_1 peak with lower energy dominated first. In addition, as the power increased, the photo-excited electrons were excited to higher energy levels, and the electrons were located on the high spin splitting band of $MoSe_2$, so the high excitation power was dominated by the IX_2 peak, which was completely consistent with the phenomenon we observed. It should be noted that as the excitation power increased, the IXs appeared to be blue shifted, which is a signature of the repulsive interaction between IXs under the dipole arrangement [1]. By combining the above analysis, we attribute the observed IX splitting to the spin-splitting of the monolayer $MoSe_2$ conduction band.

To further support the origin of IXs, we calculated the band structure of the HS by density functional theory. Figure 4 shows the energy band structure diagrams of four different stacking modes of $MoS_2/MoSe_2/WSe_2$ HS, and the four different stacking modes are represented by AA, AB, BA, and BB, respectively. Three different types of interlayer excitons IX_a, IX_b, and IX_c can be formed in trilayer type-II $MoS_2/MoSe_2/WSe_2$ HS, which are derived from $MoSe_2/WSe_2$, $MoS_2/MoSe_2$, and the longer-distance MoS_2/WSe_2 bilayers, respectively. As shown in Fig. 4(a), it can be obtained that the energies of the IXs formed among $MoSe_2/WSe_2$, $MoS_2/MoSe_2$, and the longer distance MoS_2/WSe_2 bilayer structure are 1.26, 0.61, and 0.31 eV, respectively. The calculated bandgap of the $MoSe_2/WSe_2$ bilayer at the K point is 1.26 eV, which is almost consistent with the observed IX peak of 1.33 eV in our experimental results, further indicating that the observed IXs originate from $MoSe_2/WSe_2$ bilayer. Although the theoretical calculation results cannot be in perfect agreement with the experimental phenomena, they provide insights into the origin of IXs. It can be seen that the band structures in Figs. 4(a)–4(d) are basically the same for different stacking modes, indicating that different stacking modes have little effect on the energy of IXs.

To better understand the circular polarization of the HS, the polarization-resolved PL spectrum of the $MoS_2/MoSe_2/WSe_2$ HS at 6 K was studied. As shown in Figs. 5(a)–5(c), the circular polarization of excitons in the HS region could be clearly observed. When the excitation light was a negative helicity (σ^-), the PL spectra of σ^- and positive helicity (σ^+) were analyzed. The degree of PL polarization can be quantified by the helicity parameter [23, 45], and the negative helical polarizability (P_{σ^-}) is defined as Eq. (2)

$$P_{\sigma^-} = [I(\sigma^-) - I(\sigma^+)]/[I(\sigma^-) + I(\sigma^+)] \quad (2)$$

where $I(\sigma^-)$ and $I(\sigma^+)$ represent the emission intensity of negative and positive helicity [23], respectively. Similarly, when the excitation light was σ^+, we also analyzed the PL spectra of σ^+ and σ^-. The positive helical polarizability was denoted by P_{σ^+}, similar to the definition of the P_{σ^-}.

Using the σ^- light excitation, the polarization-resolved PL spectrum of the HS at 6 K and its corresponding polarizability are demonstrated in Fig. 5(a). It is obvious that the emission intensity of σ^- light was stronger than that of the σ^+ light. The emission peaks of $MoSe_2$, WSe_2, and MoS_2 in the HS PL spectrum had the largest polarizabilities at 1.59, 1.68, and 1.88 eV, respectively, and the corresponding polarizabilities were 2.64%, 10.91%, and 3.47%, respectively. Meanwhile, Fig. 5(b) displays the resolved polarized PL spectrum of the HS and its corresponding polarizability at 6 K under the σ^+ light excitation. In contrast to the situation where the σ^- light was excited, the emission intensity of the σ^- light was superior to that of the σ^+ light. The polarizabilities (P_{σ^+}) at the energies of 1.59, 1.68 and 1.88 eV were 2.37%, 11.40% and 3.91%, respectively. The difference between σ^+ and σ^- emission intensities was due to the valley optical selection rule [46–48]. When excited by the σ^- light, the photogenerated carriers were generated in the −K valley, and the electron-hole pairs were recombined to emit σ^-

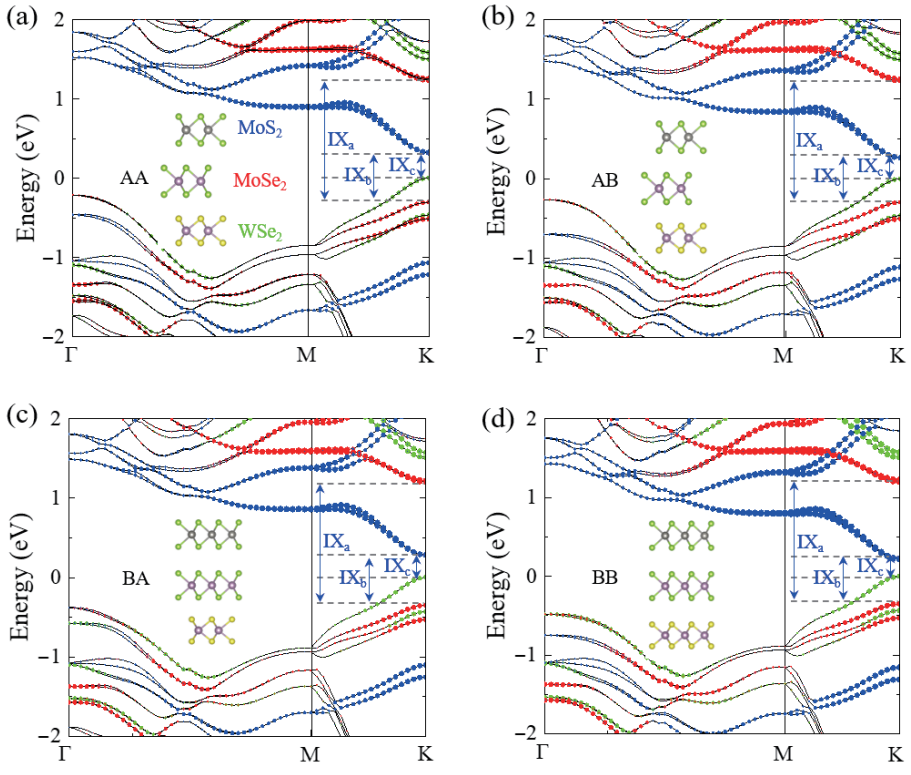

Figure 4 Density functional theory calculations of the HS. (a)–(d) Calculated the energy band structure of four different stacking patterns. AA, AB, BA, and BB represent four different stacking patterns. The atomic stacking structure of the corresponding band structure is shown in the inset. The blue, red, and green dots represent the band structures of MoS_2, $MoSe_2$, and WSe_2 monolayers, respectively.

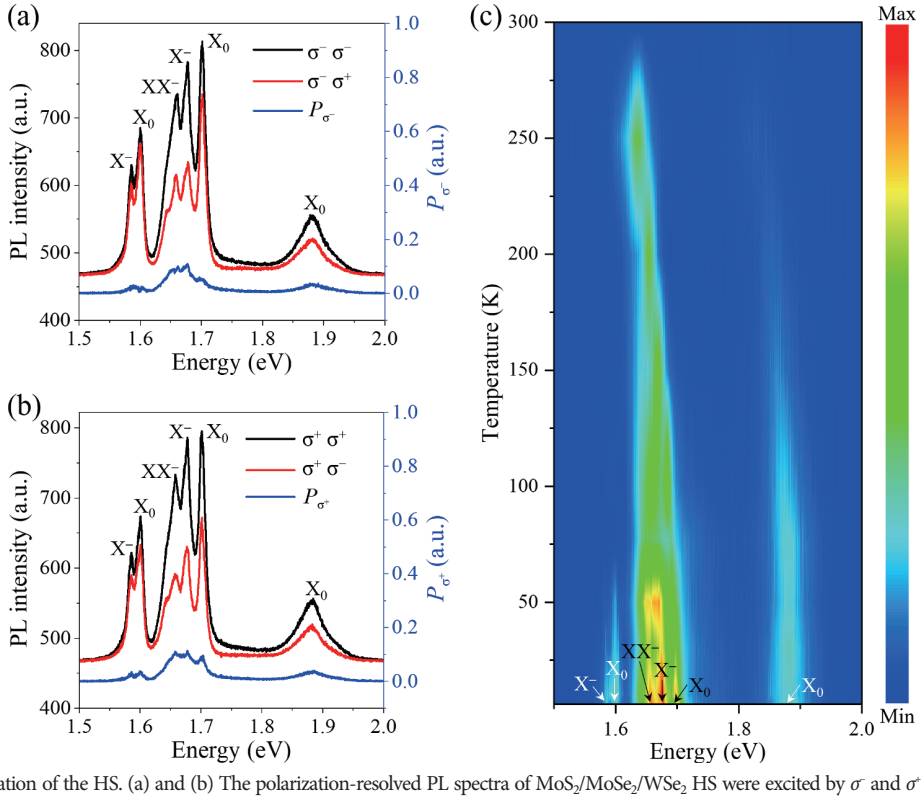

Figure 5 Valley polarization of the HS. (a) and (b) The polarization-resolved PL spectra of $MoS_2/MoSe_2/WSe_2$ HS were excited by σ^- and σ^+ light at 6 K, respectively. The left *y*-axis of (a) and (b) represents the intensity of the polarization-resolved PL spectrum of the HS, and the right *y*-axis represents the corresponding polarizability. (c) Heat map of the polarizability of the HS as a function of temperature, ranging from 6 to 300 K.

light, while there were no carriers generated in the +K valley. However, there was considerable σ^+ light emission at the +K valley due to intervalley scattering. Conversely, only the carriers at +K valley were excited when the excitation light was the σ^+ light. Figure 5(c) displays the polarization of the HS with respect to temperature, varying from 6 to 300 K. With the decrease of temperature, the polarizabilities of $MoSe_2$, WSe_2, and MoS_2 emission peaks in the HS exhibited a blue shift and gradually increased due to the decrease of the thermal disturbance of the electrons. When the temperature was 6 K, the maximum polarization rate of the WSe_2 emission peak in the HS reached 11.40%.

3 Conclusions

In summary, we have designed and demonstrated the trilayer $MoS_2/MoSe_2/WSe_2$ van der Waals HS with a Type-II alignment. The IXs in the trilayer HS were successfully observed by measuring the PL spectra. The origin of IXs is revealed by analyzing the PL characteristics in the trilayer HS as well as density functional theory calculations. According to the energy range of the IXs, we attribute the generation of the IXs to the $MoSe_2/WSe_2$ bilayer, and the varying power further proved that the splitting of the IXs originated from the conduction band spin-splitting of $MoSe_2$. Furthermore, the maximum polarizability of the WSe_2 emission peak in the HS reached 11.40% at 6 K. Our research work may provide additional insights into the exploration of new exciton physics and quantum emitters in TMD materials.

4 Experimental section

We have obtained MoS_2, $MoSe_2$, WSe_2 monolayers, and hBN sheets from bulk (HQ graphene) crystals by mechanical exfoliation. HS samples were prepared on SiO_2/Si substrates by dry transfer technique, and the TMD monolayers were stacked at random lattice matching angles. Then, the prepared HS samples were annealed at 300 °C for 5 h to reduce impurities in the samples for better contact between different TMD materials. The model number of the cryogenic refrigeration system was C04-005-044 from Cryo Industries of America. All-optical data was acquired with a WITec Alpha 300R system, using a 50× objective lens and a laser spot of nearly 1 μm. The excitation wavelength of the laser in the experiment was 532 nm (2.33 eV). Density functional theory calculations were performed using the projector augmented-wave method implemented in the VASP code.

Acknowledgment

We appreciate the support of the Hunan Province's Key Research and Development Project (No. 2019GK2233), the National Natural Science Foundation of China (No. 61775241), the Hunan Science Fund for Distinguished Young Scholar (No. 2020JJ2059), Youth Innovation Team (No. 2019012) of CSU, Hunan Province Graduate Research and Innovation Project (No. CX20190177), and the Science and Technology Innovation Basic Research Project of Shenzhen (No. JCYJ20190806144418859). Also, Y. P. L. acknowledges the support from the Central South University of the State Key Laboratory of High-Performance Complex Manufacturing Project (No. ZZYJKT2020-12). Z. W. L. thanks to the financial support from the Australian Research Council (ARC Discovery Projects, Nos. DP210103539, DP180102976, and DP130104231).

References

[1] Rivera, P.; Schaibley, J. R.; Jones, A. M.; Ross, J. S.; Wu, S. F.; Aivazian, G.; Klement, P.; Seyler, K.; Clark, G.; Ghimire, N. J. et al. Observation of long-lived interlayer excitons in monolayer $MoSe_2$–WSe_2 heterostructures. *Nat. Commun.* **2015**, *6*, 6242.

[2] Zhong, J. H.; Yu, J.; Cao, L. K.; Zeng, C.; Ding, J. N.; Cong, C. X.; Liu, Z. W.; Liu, Y. P. High-performance polarization-sensitive photodetector based on a few-layered $PdSe_2$ nanosheet. *Nano Res.* **2020**, *13*, 1780–1786.

[3] Li, J. X.; Li, W. Q.; Hung, S. H.; Chen, P. L.; Yang, Y. C.; Chang, T. Y.; Chiu, P. W.; Jeng, H. T.; Liu, C. H. Electric control of valley polarization in monolayer WSe_2 using a van der Waals magnet. *Nat. Nanotechnol.*, in press, https://doi.org/10.1038/s41565-022-01115-2.

[4] Zhong, J. H.; Wu, B.; Madoune, Y.; Wang, Y. P.; Liu, Z. W.; Liu, Y. P. $PdSe_2/MoSe_2$ vertical heterojunction for self-powered photodetector with high performance. *Nano Res.* **2022**, *15*, 2489–2496.

[5] Rasmita, A.; Gao, W. B. Opto-valleytronics in the 2D van der Waals heterostructure. *Nano Res.* **2021**, *14*, 1901–1911.

[6] Zhu, X. D.; He, J. B.; Zhang, R. J.; Cong, C. X.; Zheng, Y. X.; Zhang, H.; Wang, S. Y.; Zhao, H. B.; Zhu, M. P.; Zhang, S. W. et al. Effects of interlayer coupling on the excitons and electronic structures of WS_2/hBN/MoS_2 van der Waals heterostructures. *Nano Res.* **2022**, *15*, 2674–2681.

[7] Liu, Y. P.; Gao, Y. J.; Zhang, S. Y.; He, J.; Yu, J.; Liu, Z. W. Valleytronics in transition metal dichalcogenides materials. *Nano Res.* **2019**, *12*, 2695–2711.

[8] Baranowski, M.; Surrente, A.; Klopotowski, L.; Urban, J. M.; Zhang, N.; Maude, D. K.; Wiwatowski, K.; Mackowski, S.; Kung, Y. C.; Dumcenco, D. et al. Probing the interlayer exciton physics in a $MoS_2/MoSe_2/MoS_2$ van der Waals heterostructure. *Nano Lett.* **2017**, *17*, 6360–6365.

[9] Jin, C. H.; Ma, E. Y.; Karni, O.; Regan, E. C.; Wang, F.; Heinz, T. F. Ultrafast dynamics in van der Waals heterostructures. *Nat. Nanotechnol.* **2018**, *13*, 994–1003.

[10] Novoselov, K. S.; Mishchenko, A.; Carvalho, A.; Castro Neto, A. H. 2D materials and van der Waals heterostructures. *Science* **2016**, *353*, aac9439.

[11] Lu, N.; Guo, H. Y.; Wang, L.; Wu, X. J.; Zeng, X. C. Van der Waals trilayers and superlattices: Modification of electronic structures of MoS_2 by intercalation. *Nanoscale* **2014**, *6*, 4566–4571.

[12] Zhu, Z. Y.; Cazeaux, P.; Luskin, M.; Kaxiras, E. Modeling mechanical relaxation in incommensurate trilayer van der Waals heterostructures. *Phys. Rev. B* **2020**, *101*, 224107.

[13] Choi, C.; Huang, J. H.; Cheng, H. C.; Kim, H.; Vinod, A. K.; Bae, S. H.; Özçelik, V. O.; Grassi, R.; Chae, J.; Huang, S. W. et al. Enhanced interlayer neutral excitons and trions in trilayer van der Waals heterostructures. *npj 2D Mater. Appl.* **2018**, *2*, 30.

[14] Hao, S. C.; He, D. W.; Miao, Q.; Han, X. X.; Liu, S. Y.; Wang, Y. S.; Zhao, H. Upconversion photoluminescence by charge transfer in a van der Waals trilayer. *Appl. Phys. Lett.* **2019**, *115*, 173102.

[15] Ji, J.; Delehey, C. M.; Houpt, D. N.; Heighway, M. K.; Lee, T.; Choi, J. H. Selective chemical modulation of interlayer excitons in atomically thin heterostructures. *Nano Lett.* **2020**, *20*, 2500–2506.

[16] Yu, J.; Kuang, X. F.; Zhong, J. H.; Cao, L. K.; Zeng, C.; Ding, J. N.; Cong, C. X.; Wang, S. H.; Dai, P. F.; Yue, X. F. et al. Observation of double indirect interlayer exciton in WSe_2/WS_2 heterostructure. *Opt. Express* **2020**, *28*, 13260–13268.

[17] Rivera, P.; Seyler, K. L.; Yu, H. Y.; Schaibley, J. R.; Yan, J. Q.; Mandrus, D. G.; Yao, W.; Xu, X. D. Valley-polarized exciton dynamics in a 2D semiconductor heterostructure. *Science* **2016**, *351*, 688–691.

[18] Paik, E. Y.; Zhang, L.; Burg, G. W.; Gogna, R.; Tutuc, E.; Deng, H. Interlayer exciton laser of extended spatial coherence in atomically thin heterostructures. *Nature* **2019**, *576*, 80–84.

[19] Miller, B.; Steinhoff, A.; Pano, B.; Klein, J.; Jahnke, F.; Holleitner, A.; Wurstbauer, U. Long-lived direct and indirect interlayer excitons in van der Waals heterostructures. *Nano Lett.* **2017**, *17*, 5229–5237.

[20] Wang, Z. F.; Chiu, Y. H.; Honz, K.; Mak, K. F.; Shan, J. Electrical tuning of interlayer exciton gases in WSe_2 bilayers. *Nano Lett.* **2018**, *18*, 137–143.

[21] Deilmann, T.; Thygesen, K. S. Interlayer trions in the MoS_2/WS_2 van der Waals heterostructure. *Nano Lett.* **2018**, *18*, 1460–1465.

[22] Yuan, L.; Zheng, B. Y.; Kunstmann, J.; Brumme, T.; Kuc, A. B.; Ma, C.; Deng, S. B.; Blach, D.; Pan, A. L.; Huang, L. B. Twist-angle-dependent interlayer exciton diffusion in WS_2–WSe_2 heterobilayers. *Nat. Mater.* **2020**, *19*, 617–623.

[23] Hanbicki, A. T.; Chuang, H. J.; Rosenberger, M. R.; Hellberg, C. S.; Sivaram, S. V.; McCreary, K. M.; Mazin, I. I.; Jonker, B. T. Double indirect interlayer exciton in a $MoSe_2/WSe_2$ van der Waals heterostructure. *Acs Nano* **2018**, *12*, 4719–4726.

[24] Zhao, L. Y.; Shang, Q. Y.; Li, M. L.; Liang, Y.; Li, C.; Zhang, Q. Strong exciton-photon interaction and lasing of two-dimensional transition metal dichalcogenide semiconductors. *Nano Res.* **2021**, *14*, 1937–1954.

[25] Wang, H.; Wei, W.; Li, F. P.; Huang, B. B.; Dai, Y. Step-like band

alignment and stacking-dependent band splitting in trilayer TMD heterostructures. *Phys. Chem. Chem. Phys.* **2018**, *20*, 25000–25008.
[26] Choi, W.; Akhtar, I.; Kang, D.; Lee, Y. J.; Jung, J.; Kim, Y. H.; Lee, C. H.; Hwang, D. J.; Seo, Y. Optoelectronics of multijunction heterostructures of transition metal dichalcogenides. *Nano Lett.* **2020**, *20*, 1934–1943.
[27] Ceballos, F.; Ju, M. G.; Lane, S. D.; Zeng, X. C.; Zhao, H. Highly efficient and anomalous charge transfer in van der Waals trilayer semiconductors. *Nano Lett.* **2017**, *17*, 1623–1628.
[28] Hu, X.; Wu, J. H.; Wu, M. Z.; Hu, J. Q. Recent developments of infrared photodetectors with low-dimensional inorganic nanostructures. *Nano Res.* **2022**, *15*, 805–817.
[29] Zeng, C.; Zhong, J. H.; Wang, Y. P.; Yu, J.; Cao, L. K.; Zhao, Z. L.; Ding, J. N.; Cong, C. X.; Yue, X. F.; Liu, Z. W. et al. Observation of split defect-bound excitons in twisted WSe_2/WSe_2 homostructure. *Appl. Phys. Lett.* **2020**, *117*, 153103.
[30] Kim, K.; Yankowitz, M.; Fallahazad, B.; Kang, S.; Movva, H. C. P.; Huang, S. Q.; Larentis, S.; Corbet, C. M.; Taniguchi, T.; Watanabe, K. et al. Van der Waals heterostructures with high accuracy rotational alignment. *Nano Lett.* **2016**, *16*, 1989–1995.
[31] Hanbicki, A. T.; Currie, M.; Kioseoglou, G.; Friedman, A. L.; Jonker, B. T. Measurement of high exciton binding energy in the monolayer transition-metal dichalcogenides WS_2 and WSe_2. *Solid State Commun.* **2015**, *203*, 16–20.
[32] Tonndorf, P.; Schmidt, R.; Böttger, P.; Zhang, X.; Börner, J.; Liebig, A.; Albrecht, M.; Kloc, C.; Gordan, O.; Zahn, D. R. T. et al. Photoluminescence emission and Raman response of monolayer MoS_2, $MoSe_2$, and WSe_2. *Opt. Express* **2013**, *21*, 4908–4916.
[33] Kioseoglou, G.; Hanbicki, A. T.; Currie, M.; Friedman, A. L.; Gunlycke, D.; Jonker, B. T. Valley polarization and intervalley scattering in monolayer MoS_2. *Appl. Phys. Lett.* **2012**, *101*, 221907.
[34] Korn, T.; Heydrich, S.; Hirmer, M.; Schmutzler, J.; Schüller, C. Low-temperature photocarrier dynamics in monolayer MoS_2. *Appl. Phys. Lett.* **2011**, *99*, 102109.
[35] Wu, B.; Wang, Y. P.; Zhong, J. H.; Zeng, C.; Madoune, Y.; Zhu, W. T.; Liu, Z. W.; Liu, Y. P. Observation of double indirect interlayer exciton in $MoSe_2/WSe_2$ heterostructure. *Nano Res.* **2022**, *15*, 2661–2666.
[36] Jones, A. M.; Yu, H. Y.; Ghimire, N. J.; Wu, S. F.; Aivazian, G.; Ross, J. S.; Zhao, B.; Yan, J. Q.; Mandrus, D. G.; Xiao, D. et al. Optical generation of excitonic valley coherence in monolayer WSe_2. *Nat. Nanotechnol.* **2013**, *8*, 634–638.
[37] Li, C. C.; Gong, M.; Chen, X. D.; Li, S.; Zhao, B. W.; Dong, Y.; Guo, G. C.; Sun, F. W. Temperature dependent energy gap shifts of single color center in diamond based on modified Varshni equation. *Diam. Relat. Mater.* **2017**, *74*, 119–124.
[38] Ross, J. S.; Wu, S. F.; Yu, H. Y.; Ghimire, N. J.; Jones, A. M.; Aivazian, G.; Yan, J. Q.; Mandrus, D. G.; Xiao, D.; Yao, W. et al. Electrical control of neutral and charged excitons in a monolayer semiconductor. *Nat. Commun.* **2013**, *4*, 1474.
[39] Paur, M.; Molina-Mendoza, A. J.; Bratschitsch, R.; Watanabe, K.; Taniguchi, T.; Mueller, T. Electroluminescence from multi-particle exciton complexes in transition metal dichalcogenide semiconductors. *Nat. Commun.* **2019**, *10*, 1709.
[40] Barbone, M.; Montblanch, A. R. P.; Kara, D. M.; Palacios-Berraquero, C.; Cadore, A. R.; De Fazio, D.; Pingault, B.; Mostaani, E.; Li, H.; Chen, B. et al. Charge-tuneable biexciton complexes in monolayer WSe_2. *Nat. Commun.* **2018**, *9*, 3721.
[41] Hsu, W. T.; Lu, L. S.; Wu, P. H.; Lee, M. H.; Chen, P. J.; Wu, P. Y.; Chou, Y. C.; Jeng, H. T.; Li, L. J.; Chu, M. W. et al. Negative circular polarization emissions from $WSe_2/MoSe_2$ commensurate heterobilayers. *Nat. Commun.* **2018**, *9*, 1356.
[42] Bai, Y. S.; Zhou, L.; Wang, J.; Wu, W. J.; McGilly, L. J.; Halbertal, D.; Lo, C. F. B.; Liu, F.; Ardelean, J.; Rivera, P. et al. Excitons in strain-induced one-dimensional moiré potentials at transition metal dichalcogenide heterojunctions. *Nat. Mater.* **2020**, *19*, 1068–1073.
[43] Kormányos, A.; Zólyomi, V.; Drummond, N. D.; Burkard, G. Spin–orbit coupling, quantum dots, and qubits in monolayer transition metal dichalcogenides. *Phys. Rev. X* **2014**, *4*, 011034.
[44] Latini, S.; Winther, K. T.; Olsen, T.; Thygesen, K. S. Interlayer excitons and band alignment in MoS_2/hBN/WSe_2 van der Waals heterostructures. *Nano Lett.* **2017**, *17*, 938–945.
[45] Mak, K. F.; He, K. L.; Shan, J.; Heinz, T. F. Control of valley polarization in monolayer MoS_2 by optical helicity. *Nat. Nanotechnol.* **2012**, *7*, 494–498.
[46] Yu, H. Y.; Wang, Y.; Tong, Q. J.; Xu, X. D.; Yao, W. Anomalous light cones and valley optical selection rules of interlayer excitons in twisted heterobilayers. *Phys. Rev. Lett.* **2015**, *115*, 187002.
[47] Cao, L. K.; Zhong, J. H.; Yu, J.; Zeng, C.; Ding, J. N.; Cong, C. X.; Yue, X. F.; Liu, Z. W.; Liu, Y. P. Valley-polarized local excitons in WSe_2/WS_2 vertical heterostructures. *Opt. Express* **2020**, *28*, 22135–22143.
[48] Xiao, D.; Liu, G. B.; Feng, W. X.; Xu, X. D.; Yao, W. Coupled spin and valley physics in monolayers of MoS_2 and other group-VI dichalcogenides. *Phys. Rev. Lett.* **2012**, *108*, 196802.